ADVANCED MATERIALS TECHNOLOGIES
www.advmattechnol.de

Reactive Jetting of High Viscosity Nanocomposites for Dielectric Elastomer Actuation

*Asish Malas, Ehab Saleh, Maria del Carmen Giménez-López, Graham A. Rance, Tim Helps, Majid Taghavi, Jonathan M. Rossiter, Christopher J. Tuck, Ian A. Ashcroft, and Ruth D. Goodridge**

The layer-by-layer nature of additive manufacturing is well matched to the layer construction of stacked dielectric actuators, with inkjet printing offering a unique opportunity due to its droplet-on-demand capability, suitable for multi-material processing at high resolution. This paper demonstrates the use of high viscosity, multi-material jetting to deposit two-part reactive inks with functionalized nanofillers to digitally manufacture dielectric elastomers for soft robots with high precision, and shape manipulation. Graphene-based fillers, including graphene oxide (GO) and thermally reduced graphene oxides (TRGOs), have been incorporated into a polydimethylsiloxane (PDMS) matrix at low loading (below the percolation threshold). Consequently, the dielectric constant of the elastomer dramatically increases (by 97%) compared to neat PDMS, yielding a more than 20-fold increase in the electric-field induced electromechanical contraction (from 0.3 to 6.7%). This study shows that the oxygen-functionalities present in GO and TRGOs, which possess a moderate conductivity, improve the dispersion of those fillers in polymer matrices, thus significantly improving the dielectric constant of the polymer composites. Inkjet printing of high-performance, soft electroactive composites enables high-speed, reliable fabrication of monolithic artificial muscles (leading to stronger, cheaper, and more capable soft robotic devices) and provides a vital stepping stone towards fully additively manufactured soft robots.

1. Introduction

Soft robots, composed of soft and/or extensible materials, are increasingly being investigated as an alternative to their more conventional, rigid-bodied counterparts. Due to their compliant nature, soft robots offer adaptable and safe interaction with the human body and thus significant potential to healthcare applications, such as wearable assistive and rehabilitation devices and minimally-invasive surgical tools. The key requirements for the development of soft robots are the ability of the materials to undergo large deformation and simultaneously achieve high energy densities with short response times.

Dielectric elastomer actuators (DEAs) are one type of soft actuator composed of soft dielectric polymers sandwiched between two electrodes (**Figure 1**a).[1] They can be deformed through electrostatic interactions by applying a voltage difference that reduces their thickness, while increasing their area. The electrodes must be compliant so that

A. Malas,[+] E. Saleh,[++] C. J. Tuck, I. A. Ashcroft, R. D. Goodridge
Centre for Additive Manufacturing
Faculty of Engineering
University of Nottingham
Nottingham NG7 2GX, UK
E-mail: ruth.goodridge@nottingham.ac.uk

The ORCID identification number(s) for the author(s) of this article can be found under https://doi.org/10.1002/admt.202101111.

[+]Present address: Packaging Science and Technology, R&D Port Sunlight, Unilever, Quarry Road E, Bebington, Wirral, CH63 3JW, UK

[++]Present address: Future Manufacturing Processes Research Group, School of Mechanical Engineering, University of Leeds, Leeds LS2 9JT, UK

M. del C. Giménez-López
Centro Singular de Investigación en Química Biolóxica e Materiais Moleculares (CIQUS)
Universidade de Santiago de Compostela
Santiago de Compostela 15782, Spain

G. A. Rance
Nanoscale and Microscale Research Centre
University of Nottingham
Nottingham NG7 2RD, UK

T. Helps, M. Taghavi, J. M. Rossiter
Bristol Robotics Laboratory and University of Bristol
Bristol BS34 8QZ, UK

DOI: 10.1002/admt.202101111

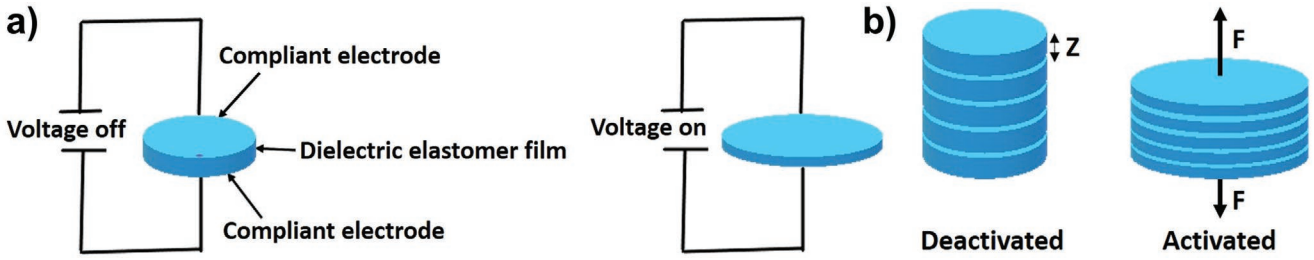

Figure 1. a) Schematic of a DEA; b) Stacked DEA in deactivated and activated states.

they can deform with the elastomer, allowing for large strains, without conductivity loss. Because of their inherent thinness, single-film DEAs typically only offer small strokes (<<1 mm). However, by stacking multiple layers of DEAs (Figure 1b), larger strokes can be achieved.[2]

The layer-by-layer nature of additive manufacturing, also commonly referred to as 3D-printing, is extremely well suited to the layer construction of stacked dielectric actuators.[3–6] Specifically, inkjet printing, which allows the precise deposition of liquid droplets on a substrate, has the capability of fabricating parts from multiple materials with the desired resolution for these thin layers. With the ability to selectively place different materials in each layer, complex structures that allow for programmable and multifunctional soft robotic actuation can be produced.

Among the available dielectric elastomers, silicones offer several advantages over acrylics due to their faster response speed (around 1000 times faster), a consequence of their very low mechanical losses,[7] in addition to their wider usable temperature range, chemical inertness, very low toxicity, and resistance to oxygen, ozone, and sunlight.[8] However, one of the main obstacles in the advancement of compliant DEAs is the high electric fields required to achieve useful actuation, which can exceed 400 MV m^{-1}.[9] In order to lower the activation voltage without either reducing the actuator's performance or increasing the modulus of the thin film, the film thickness must be decreased, or the dielectric constant of the thin film increased, typically by introducing high dielectric constant fillers into the dielectric elastomer matrix. For example, Zhang et al. reported an increase in the dielectric constant of a silicone elastomer from 3.27 to 5.85 with the incorporation of 20% of an organic filler.[10] Liu et al.[11] fabricated a silicone elastomer containing $BaTiO_3$ and reported a significant increase in the dielectric constant from 3 (silicone elastomer) to 8.5 (10 wt.% $BaTiO_3$ loaded composite). However, the drawback of using such a high loading of dielectric constant filler is that Young's modulus of the composite film tends to increase considerably, resulting in a decreased actuation strain and the need for increased driving voltage.[12]

In contrast, when an increase in dielectric permittivity comes with a reduction in Young's modulus, a synergistic effect on lowering the driving voltage is observed.[13–15] For example, Risse et al. blended a cyanopropyl-functional polydimethylsiloxane (PDMS) with a PDMS matrix, where the functionalized PDMS acted as both a high dielectric constant filler and a plasticizer. The combination of increased dielectric constant and decreased Young's moduli resulted in an improved electromechanical actuation strain response.[13] Tian et al. prepared silicone dielectric elastomer nanocomposites with thermally expanded graphene nanoplatelet fillers by solution mixing.[14] They reported an increase in the dielectric constant from 3.1 to 18.3 (at 10^3 Hz) at 1.6 wt.% loading and observed a smaller increase in dielectric loss and Young's modulus for the nanocomposite film. Using a melt blending method, Romasanta et al. developed an insulator nanocomposite film of PDMS filled with functionalized graphene sheets which showed a tenfold increase in dielectric constant (at 10 Hz) with a 2 wt.% loading, while maintaining low dielectric losses and good mechanical properties.[15]

3D reactive inkjet printing of high viscosity PDMS-based dielectric elastomers containing carbon-derived nanofillers would therefore be a step towards printing robust and high-performance stacked dielectric actuators for soft robots. However, up to now, conventional inkjet printing has been limited to low viscosity inks of up to 30 mPa s governed by the ratio of the Weber and Reynolds numbers of the ink as described by Ohnesorge.[16] Inkjet printing of nanocomposite inks has been reported using iron oxide nanoparticles in an acrylic photocurable carrier; inks with viscosities around 19 mPa s were jetted successfully, whereas inks with higher viscosities showed unstable jetting behavior.[17] To reach a viscosity level suitable for conventional inkjet printing, Sturgess et al.[18] modified the silicone viscosity using 40 wt.% octyl acetate in addition to heating the inks to 60 °C. This approach, however, limits the range of materials that can be inkjet-printed and further limits the amount of filler that can be used to formulate functionalized composites. Elahe Jabari et al.[19] produced graphene-based nanocomposites by additive manufacturing to create a highly conductive silicone-graphene structure and addressed the deployment and characterization of a piezoelectric-pneumatic material-jetting (PPMJ) process. Wallin et al.[20] reviewed additive manufacturing of soft robotic systems, highlighting the potential of inkjet printing but drawing attention to the limitations to date of processing high viscosity inks.

This work reports, for the first time, on the 3D reactive inkjet printing of high viscosity PDMS and PDMS-based nanocomposites containing carbon-derived nanofillers using non-conventional high viscosity multi-material jetting apparatus to deposit two-part reactive inks, as illustrated in **Figure 2**. The high viscosity PICO Pμlse jetting system, further described in the experimental section, uses a piston driven by a piezoelectric actuator which hammers an ink cavity allowing for jetting inks with viscosities over 10 000 mPa s.[21] Exfoliated graphene oxide (GO) powder was synthesized from graphite (G) and then reduced at both 400 and 1000 °C to control the extent of surface functionalization and degree of graphitization,[22,23] yielding thermally reduced graphene oxides (TRGOs) TRGO400 and TRGO1000, respectively. These temperatures were chosen to investigate the impact of functional group content and graphitic stacking on its distribution in PDMS as this would likely affect its actuator properties. PDMS pre-polymer ink was combined with one

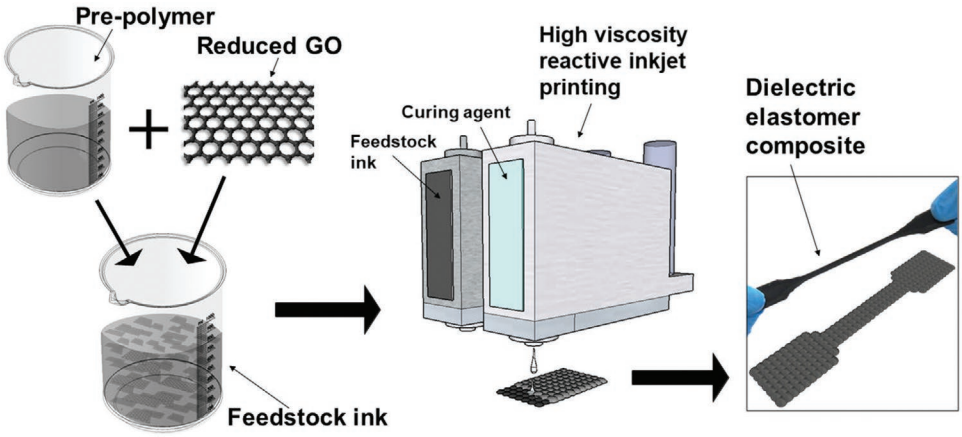

Figure 2. Schematic diagram of high viscosity reactive inkjet printing of PDMS-nanocomposites.

of four fillers (G, GO, TRGO400, or TRGO1000) at loadings of 0.75 and 1.5 wt.% to yield PDMS-0.75:G, PDMS-0.75:GO, PDMS-0.75:TRGO400, PDMS-0.75:TRGO1000, and PDMS-1.5:G, PDMS-1.5:GO, PDMS-1.5:TRGO400, PDMS-1.5:TRGO1000, respectively. Low loadings were used in the formulations to avoid reaching the percolation threshold, which increases the dielectric constant, while avoiding an increase of the modulus of the inkjet-printed composite materials, and thus enabling a flexible material with increased electromechanical actuation to be achieved. Upon printing, these were renamed P-0.75:G, P-0.75:GO, P-0.75:TRGO400, P-0.75:TRGO1000, and P-1.5:G, P-1.5:GO, P-1.5:TRGO400, P-1.5:TRGO1000, respectively.

2. Results and Discussion

2.1. Characterization of Fillers

The successful oxidation of G to GO, and the controlled thermal reductions of GO to TRGOs, was confirmed by a combination of XRD, FTIR Spectroscopy and FEG-SEM (Figure S1, Supporting Information), XPS (Figure S2, Supporting Information), and Raman spectroscopy (Figures S3 and S4 and Table S1, Supporting Information).

2.2. Inkjet Printing of PDMS and PDMS-Nanocomposites

Neat prepolymer and prepolymer composites containing the graphene-based fillers at 0.75 and 1.5 wt.% loadings (Parts A of the two-part reactive inks) were successfully inkjet-printed using a PICO Pμlse system with no inconsistency observed during the printing process. As an example, optical images of jetted PDMS Part A/TRGO ink droplets on a glass substrate and a printed sample are shown (**Figure 3**a–d).

2.3. Filler Dispersion in the 3D Printed PDMS Nanocomposites

The XRD pattern of neat printed PDMS (Figure 3e) contains a broad peak at $2\theta = 12.5°$, corresponding to a d-spacing of 0.7 nm and indicating the partially crystalline nature of PDMS, whilst a broad peak at around $2\theta = \approx 23°$ was due to the amorphous PDMS.[24] For the inkjet-printed filled PDMS nanocomposites, the diffraction peak of GO and TRGOs disappeared in their respective XRD patterns, which indicates that GO and TRGOs were partially exfoliated in the PDMS matrix.[25–27]

Representative TEM images of the inkjet-printed nanocomposites (1.5 wt.% loading) are shown (Figure 3f–h). GO sheets in P-1.5:GO (Figure 3f) were found agglomerated in the PDMS matrix, likely due to the incompatibility between the nonpolar PDMS and polar GO. For P-1.5:TRGO400 (Figure 3g), the extent of dispersion of TRGO sheets in PDMS was improved compared to GO due to the less polar nature of TRGO400 than GO. For P-1.5:TRGO1000 (Figure 3h), TRGO sheets were not located everywhere in the sample, indicating an inhomogeneous dispersion in the PDMS matrix due to the restacking of more reduced graphene sheets in the matrix. TRGO400 was more homogeneously dispersed in the PDMS matrix than TRGO1000. This is consistent with Raman images (**Figure 4**) which also show TRGO400 sheets to be more uniformly dispersed in PDMS compared to TRGO1000. Whilst the obtained Raman spectra represent a clear superposition of the individual component spectra, that is, PDMS (Figure S6, Supporting Information) and the graphitic nano-carbon, it is important to note that due to the strong overlap of the C—H asymmetric bending mode at 1410 cm^{-1} in PDMS and the D band at ≈1350 cm^{-1} in the nano-carbon, it was not possible to quantitatively appraise any changes in the graphitic ordering within the carbon phase itself induced during printing.

To quantitatively evaluate the dispersion of the TRGO400 and TRGO1000, the Raman map images of both samples (P-1.5:TRGO400 and P-1.5:TRGO1000) were analyzed by integrating the intensity of the horizontal pixels of the map to plot a representation of the dispersion within the samples, as described in the Supporting document (Figure S7, Supporting Information).

2.4. Mechanical and Dynamic Mechanical Testing of PDMS based Nanocomposites

2.4.1. Tensile Properties

The tensile properties of inkjet-printed PDMS and its nanocomposites containing G, GO, TRGO400, and TRGO1000 (0.75

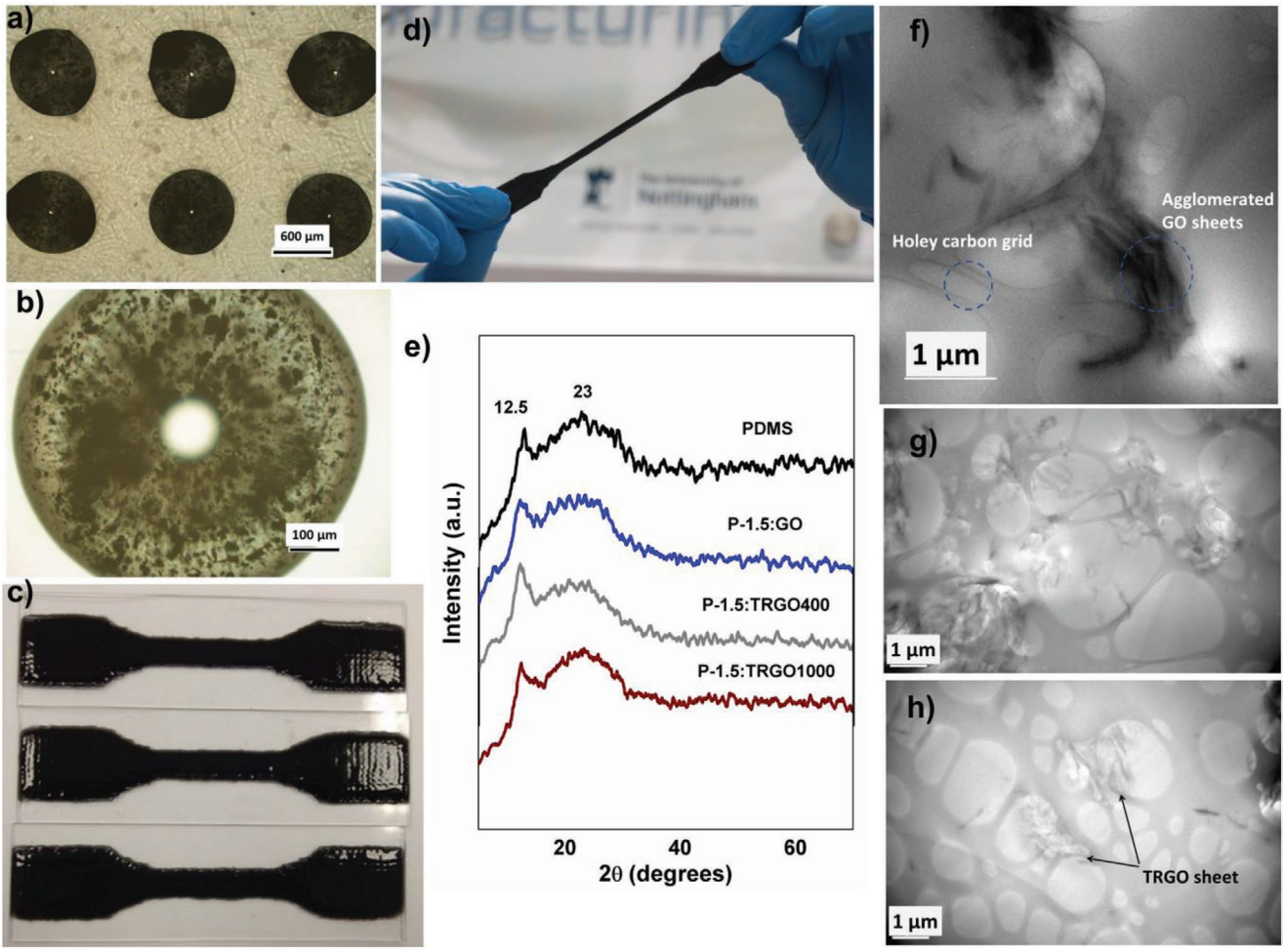

Figure 3. a,b) Optical microscope images of PICO PµIse jetted PDMS Part A/TRGO1000 (1.5 wt.%) droplets onto a glass substrate, at different magnifications (a) 5x, (b) 20x; c) A typical printed PDMS-TRGO sample (P-1.5:TRGO400) and d) demonstrating the stretchable nature of the material; e) XRD patterns of inkjet-printed nanocomposites (1.5 wt.% loading); TEM images of f) P-1.5 GO, g) P-1.5:TRGO400, and h) P-1.5:TRGO1000.

and 1.5 wt. %) are shown in **Figure 5**. From this, it is clear that Young's modulus of neat PDMS increased with the addition of TRGOs, whereas the tensile strength decreased. The Young's Modulus of P-0.75:TRGO400 and P-1.5:TRGO400 was 64 and 83% higher, respectively, than the neat printed PDMS, while P-0.75:TRGO1000 and P-1.5:TRGO1000 exhibited a 21 and 45% increase, respectively, in modulus compared to neat printed PDMS. This improvement in the elastic modulus of the TRGO-containing PDMS-based nanocomposites can be explained by the fact that the well-dispersed stiffer TRGO layers share a fraction of the total load and restrict the PDMS chain mobility through relocating stress and generating shear deformation.[28] Zaman et al.[29] and Izzuddin et al.[30] investigated the effect of graphene platelets on the mechanical properties of epoxy resin and they also observed that the modulus of the nanocomposites increased with a corresponding increase in loading, whereas the tensile strength decreased.

It can also be observed that both the Young's modulus and tensile strength of P-G and P-GO were decreased with the filler loading which was due to poor dispersion of fillers. For P-G, it is very difficult for the polymer (PDMS) chains to intercalate between the graphene sheets of G as the *d*-spacing of G is too small, resulting in poor dispersion of G in PDMS, as evidenced by Raman imaging (Figure S5, Supporting Information), and poor mechanical properties of the respective printed nanocomposite.[31] For P-GO, the poor mechanical properties were due to the poor dispersion of polar GO in nonpolar PDMS, as seen in electron microscopy (Figure 3f) and spectroscopic imaging (Figure S5, Supporting Information).

The tensile strength of all the inkjet-printed PDMS nanocomposites decreased with the addition of different fillers, which may be due to the partial aggregation of the filler nanosheets in the PDMS matrix that leads to the creation of a weak point in the PDMS matrix, therefore decreasing the strength of the elastomer.[32]

2.4.2. Dynamic Mechanical Thermal Analysis

Figure 6 shows the temperature-dependent storage modulus (E′) and tan δ of the printed samples (0.75 and 1.5 wt.% loading). The P-TRGOs show a common trend of increasing storage modulus with a corresponding increase in filler content, which was due to the better reinforcing effect exerted by

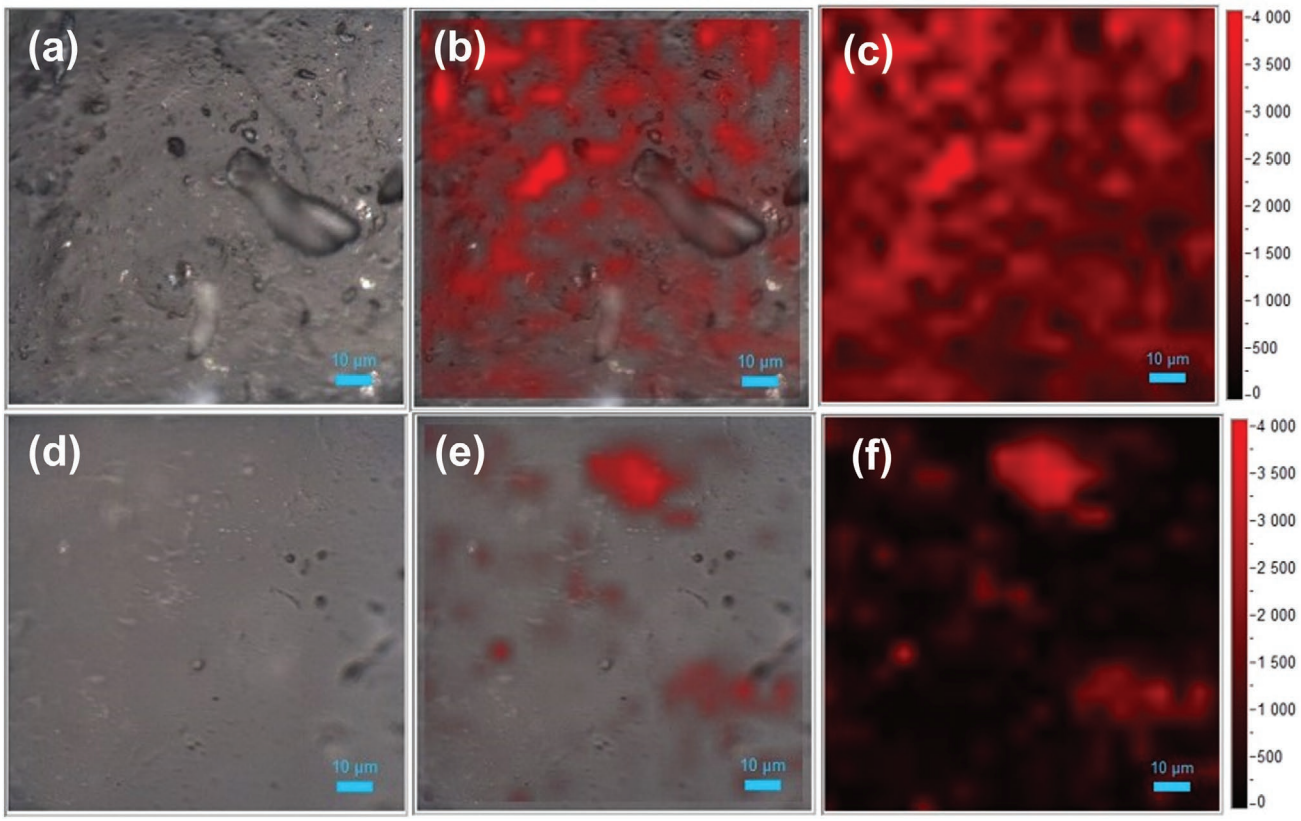

Figure 4. Raman spectroscopic imaging of a–c) P-1.5:TRGO400 and d–f) P-1.5:TRGO1000. The Raman maps (c,f), overlaid on the optical micrographs (b,e), show the variation in intensity of the G band in the Raman spectra of thermally reduced GO (red) with spatial location, not visible in optical micrographs alone (a,d). The intensity bar in (c) and (f) relate to the intensity of the G band in the spectra of the TRGO fillers (in counts).

the well-dispersed TRGOs in the PDMS matrix, as observed from TEM and Raman images. E′ is further correlated with the elastic response in the molecular level of the polymer nanocomposites, demonstrating the stiffness of the composite. The gradual improvement of E′ with an increase in TRGO loading was due to the mechanical limitation imparted by increasing filler concentration contained in the viscoelastic PDMS matrix.[33] The reduction of E′ (for PDMS and P-TRGOs) with an increase in temperature was due to the softening of the elastomer matrix and commencement of the relaxation mechanism.[34] As a result of the poor dispersion of G and GO in the PDMS matrix, P-G and P-GO exhibited a decrease in storage modulus compared to printed PDMS.

Tan δ symbolizes the ratio of the viscous to elastic response of a viscoelastic polymer or specifically the mechanical energy dissipation capability of the polymer. The tan δ peak denotes the ratio of the dissipated mechanical energy to the mechanical energy stored per cycle of sample deformation at the glass

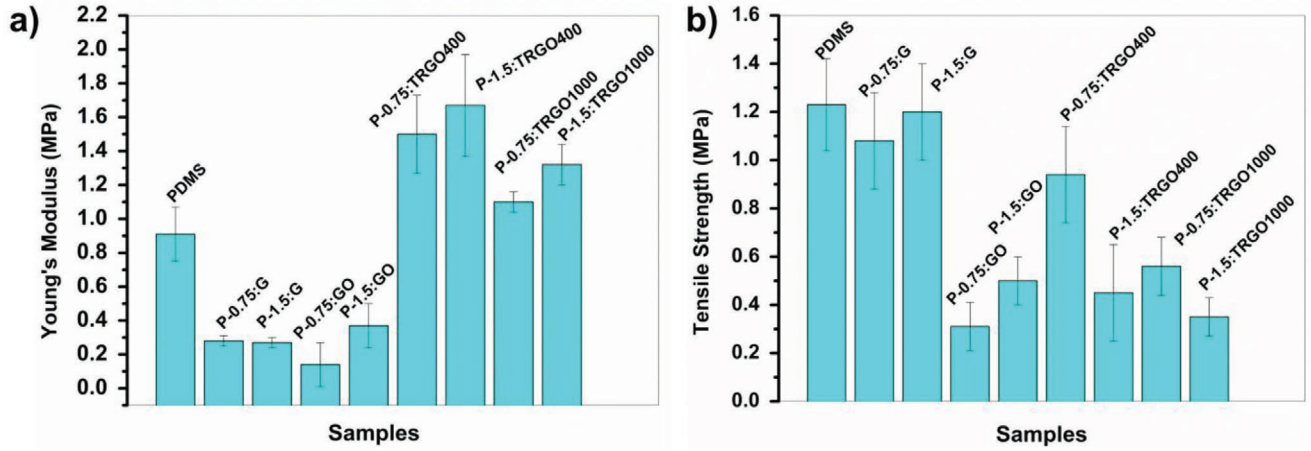

Figure 5. a) Young's modulus and b) tensile strength of the inkjet-printed nanocomposites.

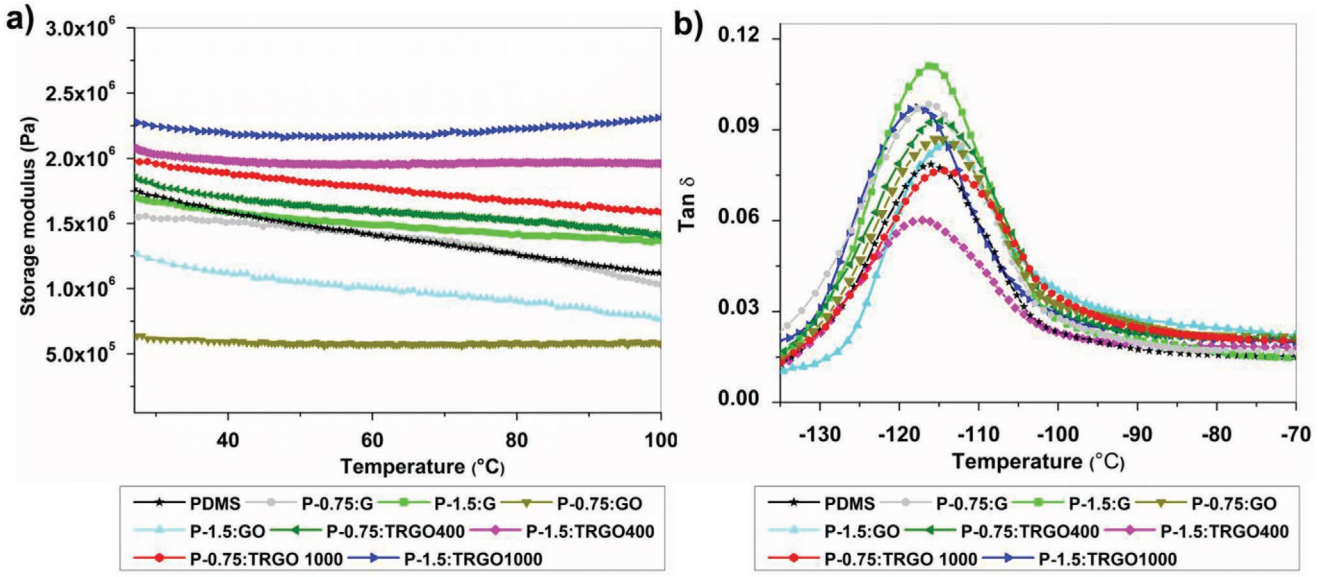

Figure 6. Temperature dependency of a) storage modulus and b) Tan δ of the inkjet-printed PDMS and its nanocomposites.

transition temperature. The glass transition temperatures (T_g) of the printed nanocomposites were determined from the temperature corresponding to the maximum in tan δ. It can be observed that the glass transition temperature of P-G remained almost unchanged, whilst P-GO increased compared to printed PDMS and with increasing filler loading due to the restriction of segmental mobility of the PDMS by the GO filler. For the P-TRGOs, T_g was increased for 0.75 wt.% loading compared to neat printed PDMS. Unexpectedly, T_g was decreased with an increase in loading for the printed P-1.5:TRGO 400 and 1000 nanocomposites. The dispersed nanoparticles (TRGOs at 1.5 wt.% loading) could interfere with the radius of gyration of the polymer chain, increasing the free volume, and thus acting like a plasticizer that results in a decrease in T_g.[35,36] Another reason for the decrease in T_g is that the nanoparticles with higher loading in PDMS interfered with the extent of crosslinking of PDMS.

2.5. Electrical and Electro-Mechanical Testing of PDMS based Nanocomposites

2.5.1. Dielectric Properties of Inkjet Printed PDMS based Nanocomposites

The dielectric constant and loss tangent (tan δ), measured at room temperature, of the inkjet-printed neat PDMS and P-G, P-GO, and the P-TRGOs are shown in **Figure 7**. The dielectric constant of materials is the measure of the ability of a material to store electric energy in an electric field. The dielectric constant was significantly increased (considering the low filler weight fraction of different fillers) by incorporating GO and different TRGO fillers. The dielectric constant spectra for the printed composites containing different TRGOs exhibited a smooth and frequency-independent behavior in the total frequency range.

It was clearly observed that the dielectric constant of P-0.75GO decreases with an increase in frequency. This can be interpreted on the grounds of decreased polarization with increasing frequency. Conventionally, polarization of a dielectric insulator is the sum of dipolar, electronic, ionic, and interfacial polarization contributions. All the different polarizations respond conveniently to the time-varying electric field at lower frequency, but the various polarization contributions separate out as the frequency of the electric field increases which results in a decrease in the net polarization of the material and causes a decrease in the magnitude of the dielectric constant at a higher frequency.[37] This anomaly is a conventional characteristic of percolative composites filled with graphene or reduced GO nanosheets, as reported in previous studies.[38,39] In this study, the dielectric constant (@1kHz) of inkjet-printed nanocomposites was increased by 48, 35, and 97% for P-1.5:GO, P-1.5:TRGO1000, and P-1.5:TRGO400, respectively, compared to neat printed PDMS. The electric charge for the composites of different TRGOs (both 0.75 and 1.5 wt.%) remained restricted to the isolated graphene sheets by the insulating PDMS matrix, which resulted in a significantly smaller increase in dielectric loss for those composites.[15] For polymer composites (multicomponent system) based on partially crystalline PDMS and conducting TRGOs (highly polarizable) nanofillers (heterogeneous system), the increase in dielectric constant was due to the Maxwell–Wagner–Sillars (MWS) interfacial polarization associated with the reorientation of interfacial charges (e.g., electrons and holes accumulated at interfaces).[40] As stated in the MWS effect,[41] when electric voltage is applied across the two-material interfaces, charges can be concentrated at the interface between two dielectric materials with dissimilar relaxation times ($\tau = \varepsilon/\sigma$, where τ is the relaxation time, ε is the dielectric permittivity and σ is the conductivity). From this perspective, the high dielectric constant (higher interfacial polarization) for the polymer nanocomposites can be achieved by increasing the contrast in conductivity (for conducting nanoparticles) or dielectric constant (for ceramic

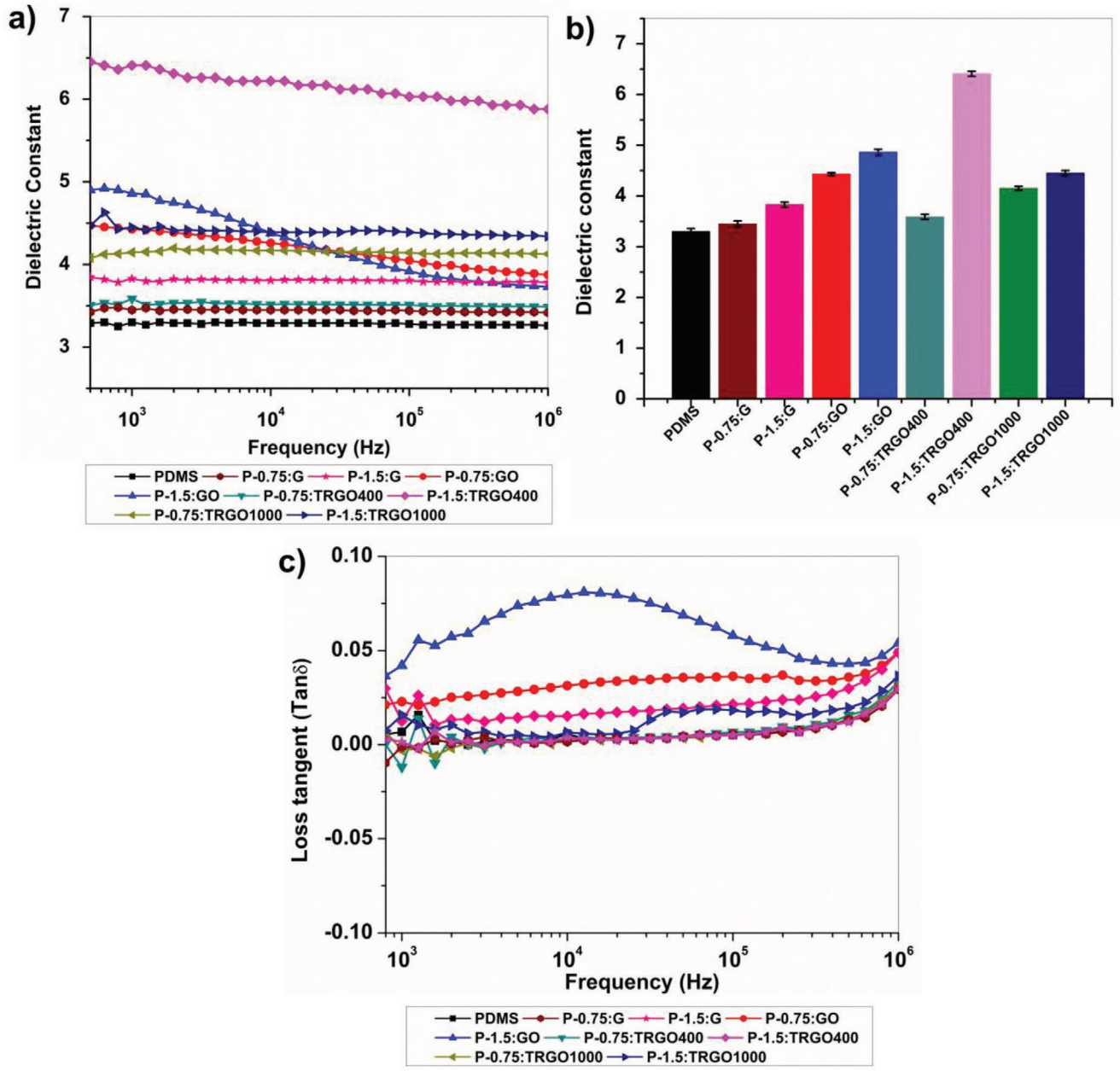

Figure 7. a) The dielectric constant vs frequency, b) dielectric constant at 1kHz, and c) dielectric loss vs frequency of the printed PDMS-based nanocomposites.

nanoparticles) between nanofiller and polymer matrix.[42] The loss tangent or tan δ is described as the ratio of the imaginary part of the dielectric constant to the real part or more specifically the ratio of the electrical energy lost to the energy stored. The loss factor (tan δ) increased from 0.006 (neat printed PDMS) to 0.040 for P-1.5:GO and moderately increased to 0.010 for both P-1.5:TRGO400 and P-1.5:TRGO1000 nanocomposites at 1 kHz. The leakage current generally leads to a significant loss factor when the conductive fillers having high aspect ratio are used due to their low percolation threshold.[43,44] This maintained dielectric constant for most of the compositions at a broad frequency range of 10 Hz to 1MHz is an indication of a broad actuation frequency range as the actuation pressure is a function of dielectric constant and electric field. However, this actuation frequency range is also a function of the natural damping of the materials which will have an impact on the performance at high frequencies and is an area of further research.

2.5.2. Electromechanical Properties of the Printed PDMS based Nanocomposites

In order to evaluate the actuation performance of the printed PDMS nanocomposites, the electromechanical properties of

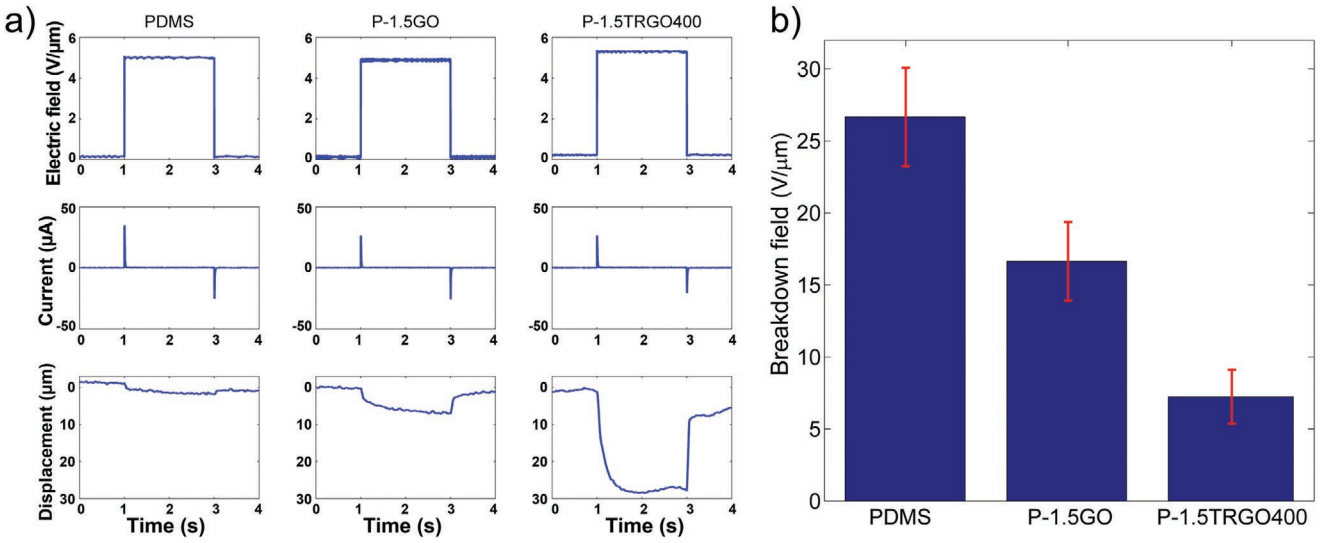

Figure 8. a) The electromechanical properties and b) breakdown threshold of inkjet-printed PDMS, P-1.5:GO and P-1.5:TRGO400.

P-1.5:TRGO400 and P-1.5:GO were measured in comparison to neat PDMS. Each sample was placed on a rigid, fixed electrode, and a second rigid, free electrode was placed on top of the sample. When an electric field was applied between the electrodes, electrostatic force (Maxwell pressure) compressed the sample, resulting in overall device contraction similar to the behavior of a DEA. Maxwell pressure is proportional to dielectric constant, and therefore a considerable improvement in electromechanical behavior was expected.

Figure 8a shows the electric field, measured current, and displacement (as a percentage of sample thickness) of neat PDMS and PDMS nanocomposites. The presence of TRGO400 induced more than a 20-fold increase in electrostatic displacement compared with neat PDMS for the same applied electric field (6.7 vs. 0.3%). The measured current shows charging and discharging behavior (observed as sharp, transient pulses in measured current when voltage is applied and removed) and negligible continuous current flow, indicating good insulation between the electrodes and that the device exhibits mostly capacitive behavior, further confirming the suitability of these nanocomposites for DEA applications.

The electric field was increased further until electric breakdown occurred, such that large currents began to flow through the device and capacitive behavior was no longer observed. Figure 8b shows the decrease of electrical breakdown field due to the presence of GO and TRGO.

The lateral actuation reported here outperforms similar reports of improved actuation behavior of related dielectric elastomers when the same value of electric field is applied, but shows a lower electrical breakdown threshold.[45,46] The limitation of breakdown can be an effect of the jetting mechanism where the distribution of filler in the deposited film may vary as described in the experimental section, in which an agglomeration of filler could initiate an electrical breakdown due to a close limit to filler percolation. The ability of inkjet printing to enable the additive manufacturing of multi-material 3D structures is well established,[47] this shows the potential of stacking layers of DAE sandwiched within inkjet-printed conductive electrodes to control the performance of the actuation array. This controlled performance could include amplifying, tuning, and functionally grading the actuation of the printed structures which is an area of ongoing interest for future work.

3. Conclusions

This study explored the 3D reactive inkjet printing of high viscosity two-part PDMS and its nanocomposites containing G, GO, and TRGOs. The following conclusions have been drawn:

- The graphitic character along with the C:O ratio of different TRGOs was confirmed to increase by increasing the temperature of heat treatment from 400 to 1000 °C. The C:O ratio in TRGO400 and TRGO1000 was increased from 2.0:1 (for GO) to 6.5:1 and 15.1:1, respectively.
- At 1.5 wt.% loading, TRGO400 was more homogeneously dispersed in PDMS than TRGO1000 or GO.
- Reactive inkjet printing of PDMS and PDMS nanocomposites is possible, despite their high viscosity, evidenced by the fabrication of multilayer cross-linked parts.
- A 21–83% increase in Young's modulus (tensile) at ambient conditions and a 5–29% increase in storage modulus (DMTA) at 27 °C was observed for the inkjet-printed PDMS-TRGO nanocomposites, depending on the amount of filler loading, compared to neat PDMS. TEM and Raman mapping indicate that this is due to their improved dispersion and reinforcement.
- Young's modulus (tensile), tensile strength, and storage modulus all decreased for P-G and P-GO compared to neat printed PDMS, due to poor dispersion of the fillers.
- The dielectric constant (at 1 kHz) of the inkjet-printed nanocomposites increased by 16–97%, depending on the filler, compared to neat PDMS. The inkjet-printed PDMS-TRGOs also exhibited a moderate increase from 0.006 (printed neat PDMS) to 0.01 in dielectric loss factor at 1 kHz.

- As a result of the significant increase (97%) in the dielectric constant for P-1.5:TRGO400 compared to the printed neat PDMS, the former exhibited 6.7% electromechanical displacement compared to 0.3% displacement for the latter (> 20-fold increase).

4. Experimental Section

Materials: Graphite (synthetic powder) with particle size <20 μm, as precursor to GO, was purchased from Sigma-Aldrich. Sulfuric acid (H_2SO_4) (>95%), hydrochloric acid (HCl) (37% solution in H_2O), and hydrogen peroxide (H_2O_2) (>30% w/v) solution were purchased from Fisher Scientific, (UK). Phosphoric acid (H_3PO_4), (≥85 wt.% in H_2O), potassium permanganate ($KMnO_4$) (ACS reagent, ≥99%), nitric acid (70%), 1H,1H,2H,2H-perfluoroctyltriethoxysilane (PFOTS), toluene (anhydrous), and ethanol were bought from Sigma-Aldrich. A two-part silicon elastomer kit (Sylgard 184) was purchased from Dow Corning. Sylgard 184 kit has two parts. One was Part A (viscosity≈5100 cP) which contains the base prepolymer and another was Part B containing curing agent. 10:1 (A:B) mixing ratio was required for crosslinking PDMS at room temperature. RS Pro silver (Ag) conductive adhesive paint was procured from RS Components Ltd, UK.

Synthesis of GO and TRGOs: GO was synthesized by a modified Hummer's method.[48] TRGOs were produced by annealing GO at 400 and 1000 °C under argon atmosphere.[49] Full details are provided in the Supporting Information.

Preparation of PDMS Prepolymer Ink Containing G, GO, and TRGOs: To prepare the PDMS-filler ink, the filler powder (G, GO, and TRGOs) was added to Part A (prepolymer) of the Sylgard 184 in a 10 mL glass bottle. After that, the Part A-filler mixture was manually mixed with a spatula for 1 h to disperse the filler in Part A. Part A of the PDMS containing 0.75 and 1.5 wt.% filler (G, GO, TRGO400, and TRGO1000) inks were prepared for reactive inkjetting (along with Part B) to print PDMS-filler nanocomposites thin film.

Inkjet Printing: The nanocomposite inks, as well as an unfilled PDMS ink for control purposes, were inkjet-printed using a PICO Pμlse jetting system. The jetting system consisted of a computer-controlled 3D stage (linear stage from Aerotech, UK) that controls the ejection of materials and position of PICO Pμlse micro-dispensing valves (Nordson EFD). The operation principle of the PICO Pμlse valves was based on the combination of pneumatic and mechanical actuation (non-contact mode of printing based upon drop-on-demand method). The fluid was pressurized pneumatically and injected into the jetting chamber along a fluid path. The jetting chamber can be heated up to 100 °C. At the end of the fluid path, a piezoelectric piston capped with a ceramic sealing ball oscillated in accordance with the printing signal (up to 1000 Hz), opening and closing the nozzle as a result. PDMS was typically printed using Part A and Part B inks. Base Part A was vinyl-terminated dimethyl siloxane, a pre-polymer of PDMS and Part B was a curing agent. In this work, Part A contained the filler (G, GO, or TRGOs). Base Part A prepolymer and Part B inks were jetted using two different PICO Pμlse valves (nozzle diameter 150 μm), as shown in Figure 2. The droplet spacing was set to 1200 μm for both Part A and Part B inks. Ten layers of Part A and one layer of Part B were jetted consecutively to prepare a single reactive layer. Due to the higher viscosity of Part A compared to Part B, the jetting chamber of Part A containing PICO Pμlse valve was heated to 80 °C during printing. Part B was jetted at room temperature. An air pressure of 2 bar was used for Part B, 14 bar (by using an extra high-pressure attachment to the PICO Pμlse valve) for Part A and a frequency of 200 Hz was applied for both valves for printing. Base Part A prepolymer containing G, GO, and TRGOs inks and Part B were printed using the same process. After printing one reactive layer, it was cured at 100 °C for 1 h in an oven to obtain an inkjet-printed thin film of PDMS and its composites.

Substrate Preparation: As the PDMS adheres easily to the microscopic glass side surface, a more hydrophobic fluorosilane modified glass slide was used as the substrate for printing the reactive PDMS layer. In a typical method, the microscopic glass slide was cleaned with nitric acid. Subsequently, the cleaned slide was chemically coated with 1% 1H, 1H, 2H, 2H-perfluoroctyltriethoxysilane (PFOTS) in anhydrous toluene before being-heat treated at 100 °C for 1 h in an oven.[18]

Characterization of the Fillers: Fourier transform infrared (FT-IR) spectra of GO, TRGOs, and other filler powders were recorded on a TL 9000 (PerkinElmer) instrument (Spectral range: 4000 cm^{-1} – 650 cm^{-1}). Micro Raman spectroscopy was performed using a HORIBA LabRAM HR Raman microscope equipped with an automated *xyz* stage (Märzhäuser). Spectra were acquired using a 532 nm laser at 0.3 mW power, a 100x objective, and a 300 μm confocal pinhole. To simultaneously scan a range of Raman shifts, a 600 lines mm^{-1} rotatable diffraction grating along a path length of 800 mm was employed. Spectra were detected using a Synapse CCD detector (1024 pixels) thermoelectrically cooled to −60 °C. Before spectra collection, the instrument was calibrated using the zero-order line and a standard Si (100) reference band at 520.7 cm^{-1}. The spectral resolution in this configuration was ≈1.7 cm^{-1}. For single-point measurements, spectra were acquired over the range 1000–3500 cm^{-1} with an acquisition time of 15–60 s and 8 accumulations to automatically remove the spikes due to cosmic rays and improve the signal to noise ratio. Spectra were collected from at least three random locations and averaged to give a mean spectrum. Spectra were baseline corrected using a second-order polynomial fitting model. X-ray diffraction (XRD) patterns of different fillers were recorded in a PANalytical MPD X-ray Diffractometer with Cu Kα source at a generator voltage of 40 kV, 40 mA current, and wavelength (λ) of 0.154 nm between 7°–80° at room temperature. The d-spacing of G, GO, and TRGOs were calculated from Bragg's equation:

$$n\lambda = 2d\sin\theta \tag{1}$$

where n is an integer, λ is the wavelength of the incident wave, d is the d-spacing, and θ is the scattering angle. X-ray photoelectron spectroscopy (XPS) measurements were conducted using a Kratos AXIS ULTRA with a mono-chromated Al Kα X-ray source (1486.6eV) operated at 10 mA emission current and 12 kV anode potential (120 W). A charge neutralizer filament was used to prevent surface charging. Hybrid slot mode was used to measure a sample area of approximately 0.5 mm^2. The analysis chamber pressure was better than 5×10^{-9} mbar. A wide scan at low resolution was used to estimate the total atomic percentages of the detected elements. High-resolution spectra at pass energy 20 eV with step of 0.1 eV, sweep times of 5, 10, or 20 min each were also acquired for photoelectron peaks from the detected elements and these were used to model the chemical composition. The high-resolution spectra were charge corrected to the C 1s peak set to 284.5 eV. After the linear baseline was subtracted, curve fitting was carried out using a mixed Gaussian–Lorentzian product function. Field emission gun scanning electron microscopy (FEG-SEM) images of GO and TRGOs were taken using JEOL 7100F FEG-SEM microscope.

Characterization of Inkjet-Printed PDMS based Composites: The morphology of the inkjet-printed GO and TRGOs filled PDMS nanocomposites were observed through high-resolution transmission electron microscope (JEOL 2100+ TEM). For TEM experiments, ultrathin cross-sections of the printed rubber nanocomposites were prepared using a CR-X Cryo Ultra microtome equipped with a diamond knife; the ultrathin cross-sections of the samples were subsequently mounted on copper-grid supported holey carbon films. To further probe the homogeneity of incorporation of the nano-carbons into the inkjet-printed films, Raman spectroscopic imaging was performed. This involved collecting individual Raman spectra at 5 μm intervals from an area 100 × 100 μm and the intensity of the G band (1480–1720 cm^{-1}) correlated with spatial location within the composite film. The DuoScan functionality was employed to increase the effective laser spot size, conferring a spatial resolution of ≈ 5 × 5 × 5 μm in the *x*, *y*, and *z*-directions respectively. As each individual spectrum was collected for 30 s, repeated once, each map required approximately 16 h of acquisition time. The intensity (as height) of the G band (1480–1720 cm^{-1}, red) was evaluated within each of the respective

maps using univariate analysis. Mechanical properties of the rubber composites were measured in a Universal tensile testing machine (INSTRON) under ambient conditions. Tensile stress at maximum load and Young's modulus were measured according to ASTM: D412 standard. For each batch, three samples were examined, and the results tabulated were the average values. Dynamic mechanical thermal (DMT) properties (storage modulus and glass transition temperature) of the printed neat PDMS thin film and its composites containing TRGOs were investigated using a DMA 8000 model (PerkinElmer) in tension mode at a constant frequency of 1 Hz, a strain of 0.05%, in the temperature range of –135 to 100 °C at a heating rate of 3 °C min^{-1}. To measure the dielectric constant of the printed PDMS and PDMS-based composites, the printed structures were sandwiched between two electrodes of screen-printed silver paint. The capacitance of each sample was measured between the electrodes using ModuLab XM instrument from Solartron.

The dielectric constant (ε) was calculated from the capacitance (C) values and the dimensions of the structures as follows:

$$\varepsilon = \frac{cd}{\varepsilon_0 A} \tag{2}$$

where d is the total thickness of the printed sample, ε_0 is the permittivity of free space, and A is the area of the printed sample. A maximum of three samples of printed PDMS and each composite were tested, and the results were averaged as shown in Figure 7.

For electromechanical high voltage experiment, each sample was placed on a flat lower electrode made from conductive tape on an acrylic surface. An upper electrode consisting of a 10 mm copper disc was placed on top of the sample. Thin 0.1 mm diameter enameled copper wire (CUL 100/0.10, Block, Germany) was used to connect the upper electrode to the high voltage amplifier so that the wire did not influence results. PVC insulation tape (AT7, Advance Tapes, UK) was used to line the edges of the sample to prevent arcing between the two electrodes around the side of the sample. Two high voltage amplifiers (10HVA24-BP1, UltraVolt, US) connected in series allowed a maximum applied voltage of 20 kV. In each test, both positive and negative polarity potential differences were applied to check for polarity dependence. The voltage was incrementally increased between experiments until breakdown occurred and this breakdown voltage was recorded. During each test, the displacement of the upper electrode was recorded using a laser displacement meter (LK-G402, Keyence, Japan). Control signals were generated, and data signals were captured using a data acquisition card (NI USB-6343, National Instruments, US).

Mechanical Testing: Mechanical properties of the rubber composites were measured in a Universal tensile testing machine (INSTRON) under ambient conditions. Tensile stress at maximum load and Young's modulus were measured according to ASTM: D412 standard. For each batch, 3 samples were examined, and the results tabulated were the average values.

Supporting Information

Supporting Information is available from the Wiley Online Library or from the author.

Acknowledgements

This work was funded by EPSRC Grant EP/M026388/1. The authors are grateful for the use of experimental facilities at the University of Nottingham (M.G-L, ERC-StG-679124, RTI2018-101097-A-I00) and to Dr. Michael Fay, Nicola Weston, and Emily Smith in the Nanoscale and Microscale Research Centre for assistance with TEM, microtomy and XPS, respectively.

Conflict of Interest

The authors declare no conflict of interest.

Data Availability Statement

The data that support the findings of this study are available in the supplementary material of this article.

Keywords

3D-printing, additive manufacturing, dielectric constant, inkjet printing, soft robotics

Received: August 26, 2021
Revised: December 2, 2021
Published online: January 17, 2022

[1] Z. Zhang, L. Liu, J. Fan, K. Yu, Y. Liu, L. Shi, L. Jinsong, *Proc. SPIE* **2008**, *6926*, 692610.
[2] G. Kovacs, L. Düring, S. Michel, G. Terrasi, *Sens. Actuators, A* **2009**, *155*, 299.
[3] D. Hua, X. Zhang, Z. Ji, Y. Changyou, B. Yu, Y. Li, X. Wang, F. Zhou, *J. Mater. Chem. C* **2018**, *6*, 2123.
[4] S. Shin, H. So, *Addit. Manuf.* **2021**, *39*, 101893.
[5] Q. Zhang, K. Zhang, G. Hu, *Sci. Rep.* **2016**, *6*, 22431.
[6] M. Zarek, M. Layani, I. Cooperstein, E. Sachyani, D. Cohn, S. Magdassi, *Adv. Mater.* **2016**, *28*, 4449.
[7] L. Maffli, S. Rosset, M. Ghilardi, F. Carpi, H. Shea, *Adv. Funct. Mater.* **2015**, *25*, 1614.
[8] P. R. Dvornic, R. W. Lenz, *High temperature siloxane elastomers*, Huthig and Wepf, New York **1990**.
[9] R. Pelrine, R. Kornbluh, Q. Pei, J. Jose, *Science* **2000**, *287*, 836.
[10] X. Q. Zhang, M. B. Wissler, J. R. Broennimann, G. Kovacs, *Proc. SPIE* **2004**, *5385*, 78.
[11] Y. Liu, L. Liu, Z. Zhang, J. Leng, *Smart Mater. Struct.* **2009**, *18*, 095024.
[12] D. Yang, S. Huang, Y. Wu, M. Ruan, S. Li, Y. Shang, X. Cui, Y. Wang, W. Guo, *RSC Adv.* **2015**, *5*, 70500.
[13] S. Risse, B. Kussmaul, H. Krüger, G. Kofod, *Adv. Funct. Mater.* **2012**, *22*, 3958.
[14] M. Tian, Z. Wei, X. Zan, L. Zhang, J. Zhang, Q. Ma, N. Ning, T. Nishi, *Compos. Sci. Technol.* **2014**, *99*, 37.
[15] L. Romasanta, M. Hernández, M. López-Manchado, R. Verdejo, *Nanoscale Res. Lett.* **2011**, *6*, 508.
[16] W. V. Ohnesorge, *J. Appl. Math. Mech.* **1936**, *16*, 355.
[17] E. Saleh, P. Woolliams, B. Clarke, A. Gregory, S. Greedy, C. Smartt, R. Wildman, I. Ashcroft, R. Hague, P. Dickens, C. Tuck, *Addit. Manuf.* **2017**, *13*, 143.
[18] C. Sturgess, C. J. Tuck, I. A. Ashcroft, R. D. Wildman, *J. Mater. Chem. C* **2017**, *5*, 9733.
[19] E. Jabari, F. Liravi, E. Davoodi, L. Lin, E. Toyserkani, *Addit. Manuf.* **2020**, *35*, 101330.
[20] T. J. Wallin, J. Pikul, R. F. Shepherd, *Nat. Rev. Mater.* **2018**, *3*, 84.
[21] J. Ledesma-Fernandez, C. Tuck, R. Hague, in *Proc. Int. Solid Free-form Fabrication Symp*, University of Texas at Austin, Texas **2015**, pp. 40–55.
[22] D. Yang, A. Velamakanni, G. Bozoklu, S. Park, M. Stoller, R. D. Piner, S. Stankovich, I. Jung, D. A. Field, C. A. Ventrice, R. S. Ruoff, *Carbon* **2009**, *47*, 145.
[23] H. H. Seung, *Thermal reduction of graphene oxide, in Physics and Applications of Graphene – Experiments*, (Ed: S. Mikhailov), IntechOpen, Rijeka, Croatia **2011**.
[24] G. L. Jadav, V. K. Aswal, P. S. Singh, *J. Mater. Chem. A* **2013**, *1*, 4893.
[25] H. Hu, L. Zhao, J. Liu, Y. Liu, J. Cheng, J. Luo, Y. Liang, Y. Tao, X. Wang, J. Zhao, *Polymer* **2012**, *53*, 3378.

[26] J. Liang, Y. Huang, L. Zhang, Y. Wang, Y. Ma, T. Guo, Y. Chen, *Adv. Funct. Mater.* **2009**, *19*, 2297.
[27] D. Yang, S. Yang, Z. Jiang, S. Yu, J. Zhang, F. Pan, X. Cao, B. Wang, J. Yang, *J. Membr. Sci.* **2015**, *487*, 152.
[28] I. Zaman, Q. Le, H. Kuan, N. Kawashima, L. Luong, A. Gerson, J. Ma, *Polymer* **2011**, *52*, 497.
[29] I. Zaman, T. Phan, H. Kuan, Q. Meng, L. Bao La, L. Luong, O. Youssf, J. Ma, *Polymer* **2011**, *52*, 1603.
[30] I. Zaman, H. Kuan, Q. Meng, A. Michelmore, N. Kawashima, T. Pitt, L. Zhang, S. Gouda, L. Luong, J. Ma, *Adv. Funct. Mater.* **2012**, *22*, 2735.
[31] M. Bhattacharya, *Materials* **2016**, *9*, 262.
[32] J. Fu, L. Chen, H. Yang, Q. Zhong, L. Shi, W. Deng, X. Dong, Y. Chen, G. Zhao, *Polym. Compos.* **2012**, *33*, 404.
[33] R. Huang, X. Xu, S. Lee, Y. Zhang, B. Kim, Q. Wu, *Materials* **2013**, *6*, 4122.
[34] M. S. Huda, A. K. Mohanty, L. T. Drzal, M. Misra, E. Schut, *J. Mater. Sci.* **2005**, *16*, 4221.
[35] W. Xie, J. Hwu, G. Jiang, T. Buthelezi, W. Pan, *Polym. Eng. Sci.* **2003**, *43*, 214.
[36] Y. Sun, Z. Zhang, K. Moon, C. Wong, *J. Polym. Sci., Part B: Polym. Phys.* **2004**, *42*, 3849.
[37] H. Naceur, A. Megriche, M. Maaqoui, *Orient. J. Chem.* **2013**, *29*, 937.
[38] S. K. Kumar, M. Castro, A. Saiter, L. Delbreilh, J. F. Feller, S. Thomas, Y. Grohens, *Mater. Lett.* **2013**, *96*, 109.
[39] S. Song, Y. Zhai, Y. Zhang, *ACS Appl. Mater. Interfaces* **2016**, *8*, 31264.
[40] F. Kremer, A. Schönhals, *Broad band dielectric spectroscopy*, Springer, New York **2003**.
[41] R. Tamura, E. Lim, T. Manaka, M. Iwamoto, *J. Appl. Phys.* **2006**, *100*, 114515.
[42] J. Yuan, S. Yao, P. Poulin, *Dielectric Constant of Polymer Composites and the Routes to High-k or Low-k Nanocomposite Materials*, (Eds: X. Huang, C. Zhi), Springer Cham, Switzerland **2016**, pp. 3–28.
[43] J. Yu, X. Huang, C. Wu, P. Jiang, *IEEE Trans. Dielectr. Electr. Insul.* **2011**, *18*, 478.
[44] C. Yang, Y. Lin, C. Nan, *Carbon* **2009**, *47*, 1096.
[45] D. M. Opris, M. Molberg, C. Walder, Y. S. Ko, B. Fischer, F. A. Nüesch, *Adv. Funct. Mater.* **2011**, *21*, 3531.
[46] N. Ning, Q. Ma, S. Liu, M. Tian, L. Zhang, T. Nishi, *ACS Appl. Mater. Interfaces* **2015**, *7*, 10755.
[47] E. Saleh, F. Zhang, Y. He, J. Vaithilingam, J. L. Fernandez, R. Wildman, I. Ashcroft, R. Hague, P. Dickens, C. Tuck, *Adv. Mater. Technol.* **2017**, *2*, 1700134.
[48] D. C. Marcano, D. V. Kosynkin, J. M. Berlin, A. Sinitskii, Z. Sun, A. Slesarev, L. B. Alemany, W. Lu, J. M. Tour, *ACS Nano* **2010**, *4*, 4806.
[49] N.-J. Song, C.-M. Chen, C. Lu, Z. Liu, Q.-Q. Kong, R. Cai, *J. Mater. Chem. A* **2014**, *2*, 16563.